)--/

LA-UR- 91-1654

LA-UR--91-1654

DE91 013317

Los Alamos National Laboratory is operated by the University of California for the United States Department of Energy under contract W-7405-ENG-36

TITLE: "A SLIT APERTURE FOR THE MONITORING X-RAY EXPERIMENT (MOXE)"

AUTHOR(S): James C. Lochner
William C. Priedhorsky

SUBMITTED TO: SPIE International Symposium

DISCLAIMER

Los Alamos National Laboratory
Los Alamos, New Mexico 87545

A slit aperture for the Monitoring X-ray Experiment (MOXE)

James C. Lochner & William C. Priedhorsky

Space Astronomy and Astrophysics Group
Los Alamos National Laboratory
Los Alamos, NM 87545

ABSTRACT

We have investigated a slit aperture as an alternative to the square pinhole aperture for the MOXE detectors, which are to be put on the Soviet satellite Spectrum X-Gamma. A slit offers advantages for better discrimination of sources in crowded regions, eliminates the need for support structures for the aperture window, and does not compromise the signal-to-noise (S/N) of a point source. We find that in a single 24 hr pointing of the satellite, MOXE can determine the position of a 10 mCrab source to better than 0.5° with the slit. The structure of a titanium grate which supports the detector's beryllium window constrains the slit to be 0.5 cm x 2.56 cm, oriented at an angle of 26.6° to either side of the center lines of the detector. We illustrate an arrangement of the slits on each of the six detectors which optimizes source localization for a number of pointings.

1. INTRODUCTION

The Monitoring X-ray Experiment (MOXE) is an all sky monitor to be flown on the Soviet Spectrum X-Gamma Satellite[1,2]. MOXE consists of 6 position sensitive proportional counters having a bandwidth of 2 - 12 keV. Figure 1 illustrates the basic features of each detector. Each detector has an active area of 1024 cm^2, a maximum position resolution FWHM value of 0.5 cm in each direction, and a pixel size of 0.25 x 0.25 cm. The distance from the aperture to the detector is 14.983 cm. The detector body is filled with an Xe - CO_2 gas mixture at 1.0 atm. The cone is filled with helium to provide support for the detector window.

Each detector views 1/6 of the sky and is oriented along the face of a cube, so the entire experiment provides continuous full sky coverage. MOXE serves both as a record of the X-ray sky, and as an alarm to transient events so that the other instruments on Spectrum X-Gamma may perform more detailed follow-on studies. The satellite has several x-ray telescopes on a pointed platform, with 1 - 5 pointings per day.

The experiment was originally designed with a 1 x 1 cm pinhole aperture for each detector. From the Japanese experience with a slit aperture[3], we have undertaken a re-design of the MOXE aperture. The new aperture is a 0.5 x 2.56 cm slit, oriented at an angle of 26.6°. In this paper, we shall show that the slit attains the same signal-to-noise as the pinhole, and demonstrate that the position accuracy along the long dimension of the slit is better than 0.5° for a 10 mCrab source. We shall also discuss existing features of the detector design which led to the particular size and orientation of the slit, and illustrate the different relative orientations of the slit on each of the detectors which best localize sources.

2. SIGNAL-TO-NOISE COMPARISONS

We first compare the expected signal-to-noise from a square 1.0 x 1.0 cm pinhole and from a slit. To compare apertures of the same open area, we use a 0.5 x 2.0 cm slit in the following computations, rather than the final 0.5 x 2.56 cm slit. The signal-to-noise (S/N) is given by

$$S/N = \frac{\sum \varepsilon S(x,y) A_p t}{\sqrt{\sum A_p t (\varepsilon S(x,y) + I + \Omega D \varepsilon)}}, \qquad (1)$$

where the sums are over selected detector pixels $S(x,y)$, A_p is the area of the pixel, t is the integration time, ε is the detector efficiency (which we've taken to be 1.0 for absorbed photons), I is the internal background (0.01 cts cm^{-2} s^{-1}), and

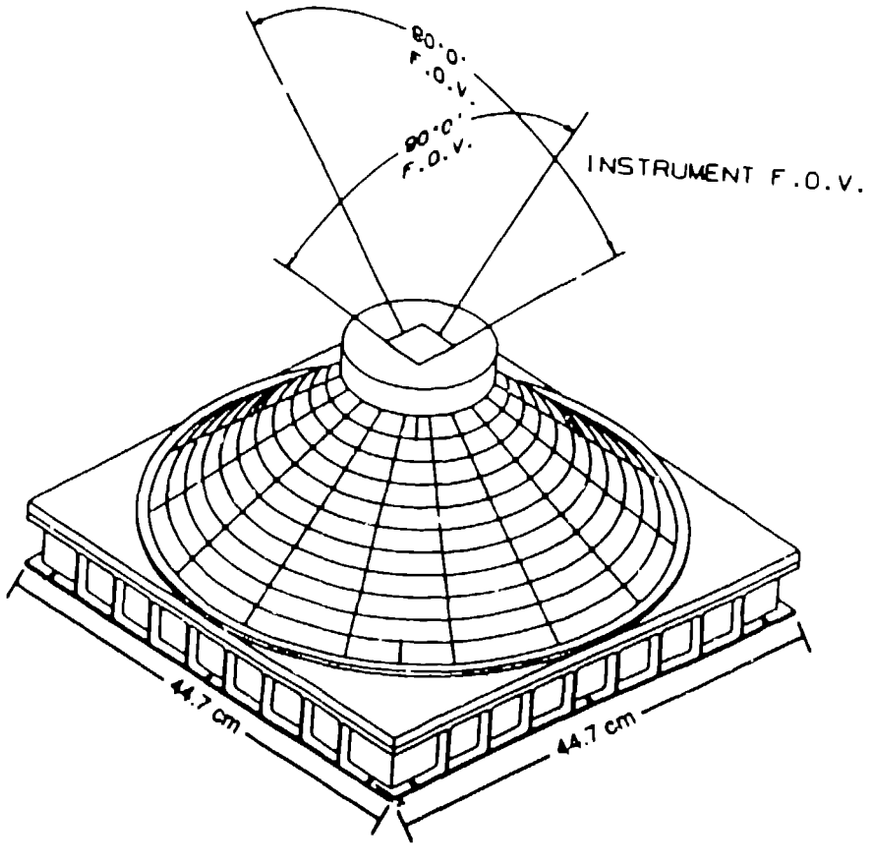

Figure 1. The MOXE detector assembly, with the original pinhole aperture. The assembly consists of the detector enclosure and the conical aperture support structure. Both the slit and pinhole apertures give 90° fields of view.

D is the diffuse sky background for a solid angle subtended by a 1 cm^2 aperture (0.01 cts cm^{-2} s^{-1}). Below we discuss details of the effects which modify the source and background counts from their incident values: the 0.5 cm FWHM spatial resolution of the proportional counter; the shadows cast by the supports for the pinhole's aperture window; absorption in the counter gas; and simple geometric effects for non-normal incidence. These effects have been digitized to the square 0.25 cm detector pixels, and have been modelled for bright and dim parallel-beam sources, and for both normal incidence and for the maximum incidence angle of 45°.

The supports for the beryllium window required for the pinhole decrease the number of photons arriving at the detector. For supports 0.05 cm wide and 0.05 cm high (required for a 1 x 1 cm pinhole and 4 mil Be window), the obscuration is 5 % in each dimension for normal incidence, giving total obscuration of 10 %. For off-axis illumination from a direction parallel to one of the supports, obscuration due to the support perpendicular to the illumination direction increases to

$$0.05(1 + \tan\theta), \tag{2}$$

where θ is the angle of incidence measured from the normal. The slit, on the other hand, does not require any support structure for the Be window, as a 0.5 cm width for any length provides adequate support for a 4 mil window.

The percentage of incident photons which register in the detector is given by absorption in the counter gas. This absorption is given by

$$A(\theta)=1-e^{-\tau d/\cos\theta} \tag{3}$$

where τ = 1.360 / cm is the absorption per unit path length in the Xe gas at 4.78 keV, and d = 1 cm is the active depth of

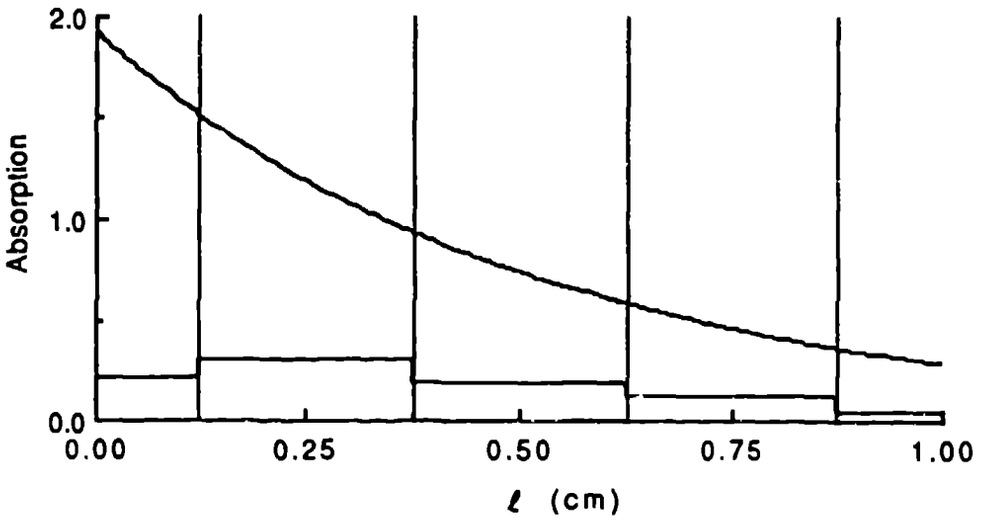

Figure 2. Absorption profile (Eq. 4) (top curve), and digitized absorption (Eq. 5) for 45° incidence and τ = 1.36 / cm. Vertical lines indiate pixel boundaries.

the detector. We have chosen 4.78 keV (just below the Xe L-edge) as the part of the 2 - 12 keV region where Xe is least absorbing. The absorption varies from $A(0°) = 0.74$ to $A(45°) = 0.85$.

At non-normal incidence, photons striking the surface of a given pixel may be absorbed in the deeper layers of neighboring pixels. This absorption profile is given by

$$\frac{\tau}{\cos\theta} e^{-\tau \ell/\cos\theta} \tag{4}$$

where ℓ is the path length. The absorption in a given pixel is then

$$\int_{\ell_1}^{\ell_2} \frac{\tau}{\cos\theta} e^{-\tau \ell/\cos\theta} d\ell = e^{-\tau \ell_1/\cos\theta} - e^{-\tau \ell_2/\cos\theta} \tag{5}$$

where ℓ_1 and ℓ_2 are locations of the pixel boundaries relative to the incident position of the incoming photon. We have modelled the incoming photons as incident at the top and center of the pixel, causing the first incident pixel to have a smaller absorption than the next pixel. Figure 2 gives the absorption profile and the digitized absorption for $\theta = 45°$. With pixel widths of 0.25 cm, the values of ℓ_1 and ℓ_2 for $\theta = 45°$ are (0,1/8), (1/8,3/8), (3/8,5/8), (5/8,7/8), and (7/8,1).

The spatial resolution of the detector causes photons deposited in one pixel to possibly register in a nearby pixel. This is modelled by convolving the incident image with a Gaussian. The intensity in a given pixel x, y is given by

$$S(x,y) = \sum_{i,j} S(x_i,y_j) g(x - x_i,\sigma) f(y - y_j,\sigma) \tag{6}$$

where $S(x_i,y_j)$ is the intensity of a directly illuminated pixel,

$$f(y-y_j,\sigma) = \frac{1}{2\pi} \int_b^a e^{-x^2/2\sigma^2} dx, \tag{7}$$

$a = y - y_j + 0.125$, $b = y - y_j - 0.125$, and $g(x-x_i,\sigma)$ is a convolution of f with the absorption profile discussed above (eq. 5). We assume a FWHM of 0.5 cm ($\sigma = 0.213$ cm). As with the absorption blur, we model this effect by assuming that flux is incident at the top and center of each 0.25 x 0.25 cm pixel.

The geometric effect for off axis illumination decreases the incident intensity and the diffuse sky background by cos θ.

With these effects included in the source and background counting rates, we construct 2-D maps of intensity for bright and dim incident sources on the pinhole and slit apertures. For each image, we select the set of 0.25 x 0.25 cm pixels which yields the best S/N using Eq. 1. For example, we get the best S/N for the 1 cm^2 aperture and a bright source at normal incidence by taking the signal from the inner 6 x 6 pixels. A smaller sample of pixels gives too little signal, while a larger sample gives too much background.

Table 1 gives the maximum S/N per second for various configurations of apertures, incidence angle, and relative illumination direction. The *Incident Intensity* is the total counts incident on the detector before obscuration or absorption effects. The total background is 1.25×10^{-3} cts $pixel^{-1}$ s^{-1}. The *Area* and *Intensity* are the total area and absorbed intensity of that set of pixels which give the best S/N. The 2.0 x 0.5 cm aperture has the 45° incidence parallel to the long dimension of the slit, and the 0.5 x 2.0 cm aperture has the 45° incidence parallel to the short dimension of the slit (see Fig. 3).

We see from Table 1 that the S/N for the slit and pinhole are comparable for a dim source of incident intensity 16×10^{-4} cts s^{-1}. The final design slit length of 2.56 cm further enhances the S/N.

Table 1
Maximum Signal-to-Noise for Aperture Configurations

Aperture	Incident Intensity (cts s^{-1})	θ (°)	Area (cm^2)	Pixel Sample	Intensity (cts s^{-1})	S/N (s^{-1})
1.0 x 1.0 cm	16.0	0	2.25	6 x 6	10.31	0.776
		45	3.75	10 x 6	8.07	0.669
	16.0×10^{-4}	0	1.00	4 x 4	7.59×10^{-4}	3.35×10^{-4}
		45	1.00	4 x 4	5.73×10^{-4}	2.45×10^{-4}
2.0 x 0.5 cm	16.0	0	4.50	12 x 6	11.87	0.813
		45	3.25	13 x 4	9.16	0.722
	16.0×10^{-4}	0	1.00	8 x 2	7.48×10^{-4}	3.30×10^{-4}
		45	1.13	9 x 2	6.03×10^{-4}	2.71×10^{-4}
0.5 x 2.0 cm	16.0	0	4.5	6 x 12	11.87	0.813
		45	5.00	8 x 10	9.50	0.721
	16.0×10^{-4}	0	1.00	2 x 8	7.48×10^{-4}	3.30×10^{-4}
		45	2.50	5 x 8	8.04×10^{-4}	2.43×10^{-4}

3. SLIT ORIENTATION & SIZE

3.1 Effect of titanium grate

We now consider the specific length and arrangement of the slit, and the relative orientation of the slits on various detectors.

A second beryllium window separates the detector from the cone assembly, and is supported by the pressure of the He in the cone and by a titanium grate (see Figure 4). The ribs in the grate are separated (center-to-center) by 0.450 in (1.143 cm), are 0.050 in (0.127 cm) wide, and vary in height from 0.350 in (0.889 cm) to 0.05 in (0.127 cm) by 0.025 in (0.0635 cm) increments. The diagonal supports are 0.125 in (0.3175 cm) wide. The ribs and diagonal supports introduce additional shadowing on the image. In the following analysis, we shall concentrate on the obscuration caused by the ribs only.

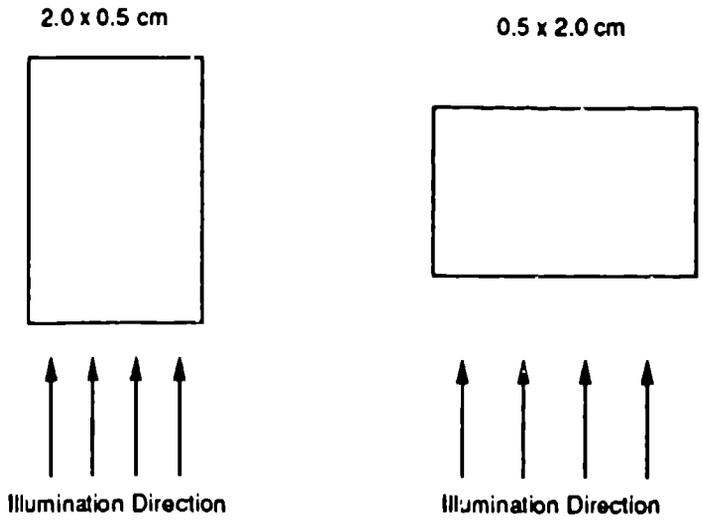

Figure 3. Relative orientation of slits and illumination directions for Table 1.

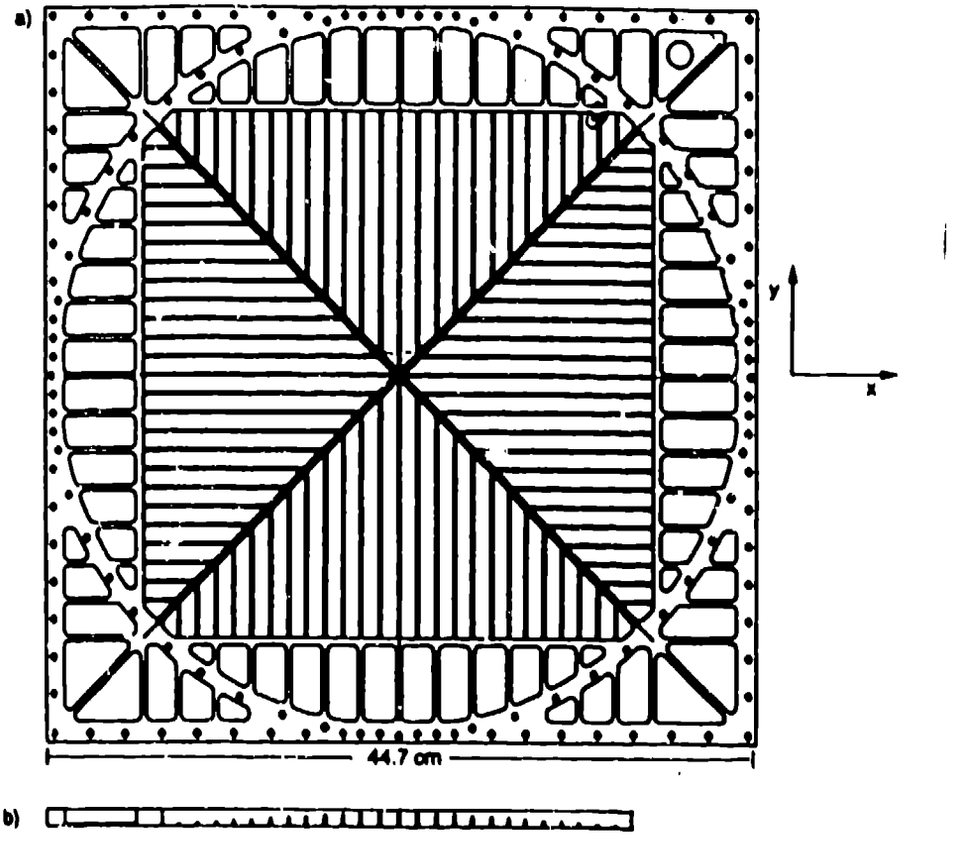

Figure 4. a) Titanium support for the detector beryllium window. b) Profile of rib heights across the grate.

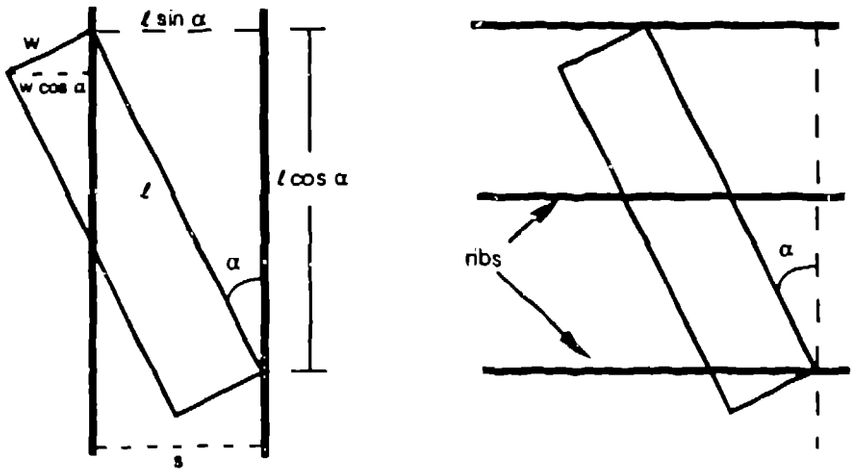

Figure 5. Orientation of the slit image relative to the ribs for fixed α.

It is desirable that the obscuration by the ribs be constant regardless of the position of the aperture image on the detector. *Assuming the ribs have zero height*, this can be accomplished by a slit of an appropriate length and at an appropriate orientation relative to the ribs. Figure 5 shows the aperture image falling in two different quadrants of the detector, and suggests that the obscuration can be made constant by always having a given number of ribs in the aperture image. Let there be only one rib in the image in the "x" orientation (as shown in the figure), and let there be n ribs in the field for the "y" orientation. From Figure 5, we have

$$\ell \sin\alpha = s \qquad\qquad \ell \cos\alpha = ns, \tag{8}$$

where s = 1.143 cm is the separation of the ribs. Quite readily,

$$\tan\alpha = 1/n. \tag{9}$$

Using n = 1 gives α = 45°, ℓ = 1.62 cm. For n = 2, α = 26.57°, ℓ = 2.56 cm. Keeping the slit width at 0.5 cm, the obscuration by these flat ribs at near normal incidence leaves an open area for each orientation of 1.14 cm^2, or 88.9 % of the aperture area. This open area is the same regardless of the exact position of the ribs in the aperture image. For comparison, enlarging the square pinhole to 1.143 cm so that one rib is always in the aperture image, the open area varies between 84.9 % and 80.7 %, due to overlap between the ribs and the pinhole's own support ribs.

We now consider the arrangement of the slits on each of the detectors. It is desirable to have the slits at different orientations relative to a fixed observer as the satellite maneuvers about its sun axis. Multiple pointings then give multiple orientations of the slit to a fixed sky position, and better position determination (as discussed in § 4). This can be achieved since the slit can be oriented 26.6° relative to either the central x or y axis of the detector. Further, from our signal-to-noise studies we saw that the signal-to-noise for a bright source will be attained in a smaller area if the illumination direction lies along the length of the slit. Thus, for the sunward detectors, a preferred placement is for the slit to point approximately toward the sun, minimizing the detector area occupied by the sun. Figure 6*a* shows the arrangement of the slits on the three sunward detectors, in which two detectors (labeled 2 and 3 in the figure) have slits pointing toward the sun. Of these three detectors, detectors 1 and 2 have slits which are orthogonal relative to a fixed observer, and the slit on detector 3 is 53.1° and 36.9° from the others. Figure 6*b* shows the slit arrangement for the anti-sunward detectors, in which the slits on detectors 4 and 5 are orthogonal. The anti-sunward detectors are placed such that detectors 1, 2 and 5 have mutually overlapping fields of view. For points along the satellite's equator, this arrangement of the slits on the sunward and anti-sunward detectors provides a great variety of orientations of the slits relative to a fixed position on the sky.

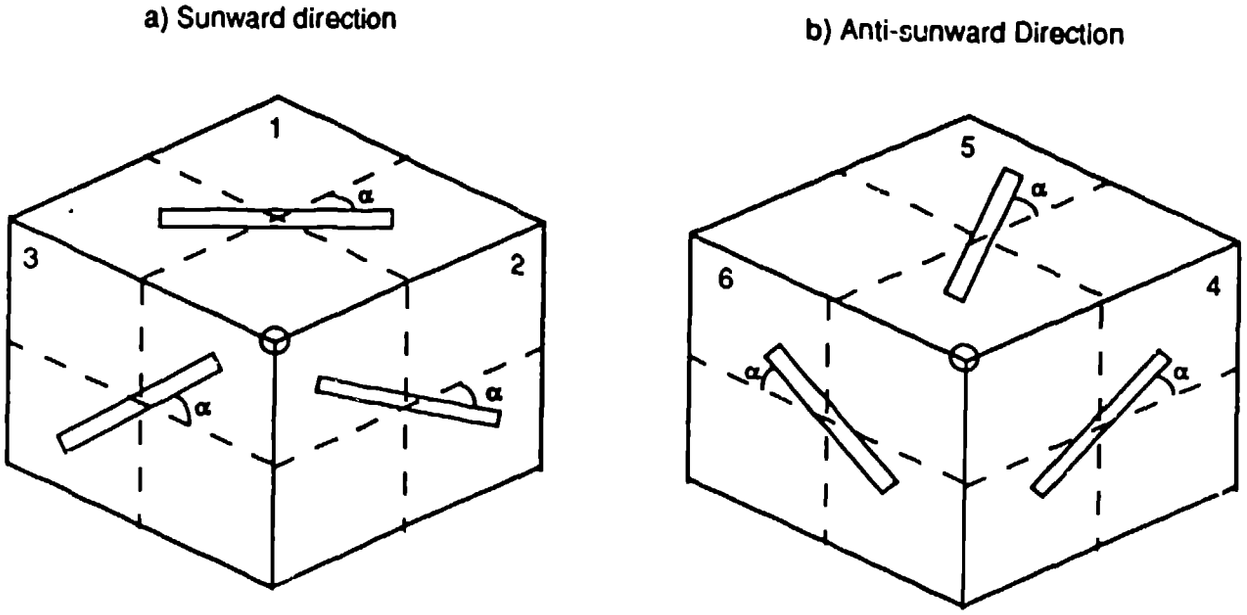

Figure 6. Arrangement of the slits for each of the MOXE detectors. The detectors are shown schematically on the faces of a cube, with the sunward / anti-sunward directions indicated by the circled vertex. For each slit, $\alpha = 26.6°$. Detectors are numbered in the order that they sweep past a position near the satellite equator.

3.2 Effect of the Height of the Ribs

Shadows are cast by the ribs of the titanium grate onto the detector because of both their width and height. The above discussion considered only the width of the ribs in determining the amount of obscured area. A rib of height h casts a shadow of width

$$w_s = h \sin\phi \tan\theta , \tag{10}$$

where the direction of radiation is an incident angle θ from the z axis and an azimuthal angle ϕ from the x axis. Measured from the center of the detector, x and y positions on the detector are given by

$$x = f \cos\phi \tan\theta \qquad\qquad y = f \sin\phi \tan\theta , \tag{11}$$

where $f = 14.983$ cm is the distance from the aperture to the detector. For illuminations from the negative x direction, this gives shadows of widths

$$w_s = \frac{|y|}{f} h. \tag{12}$$

Table 2 lists the total width of the rib plus its shadow for each of the ribs, and the fraction of the open area of the aperture. (The shadow widths are computed at the *edge* of the rib.) For the "x" orientation of the slit, the fraction of the open area remaining when one rib is fully in the aperture image is

$$T = 1 - \frac{5}{2} \frac{w \cos\alpha}{\ell w} (w_s + w_r), \tag{13}$$

where w is the width of the slit, and w_r is the fixed width of the rib. (This uses the area of the parallelogram which the rib makes when its maximum length lies in the aperture image.) With our values of α and ℓ, this becomes

$$T = 1 - \frac{(w_s + w_r)}{1.143}. \tag{14}$$

Table 2
Width of Obscured Regions

Rib Position (cm)	Obscured Width (cm)	Fraction Open Area
0.0	0.127	0.889
1.206	0.193	0.831
2.349	0.246	0.784
3.492	0.290	0.746
4.635	0.323	0.717
5.778	0.347	0.696
6.921	0.362	0.684
8.064	0.366	0.680
9.207	0.361	0.684
10.350	0.346	0.697
11.493	0.322	0.718
12.636	0.288	0.748
13.779	0.244	0.787

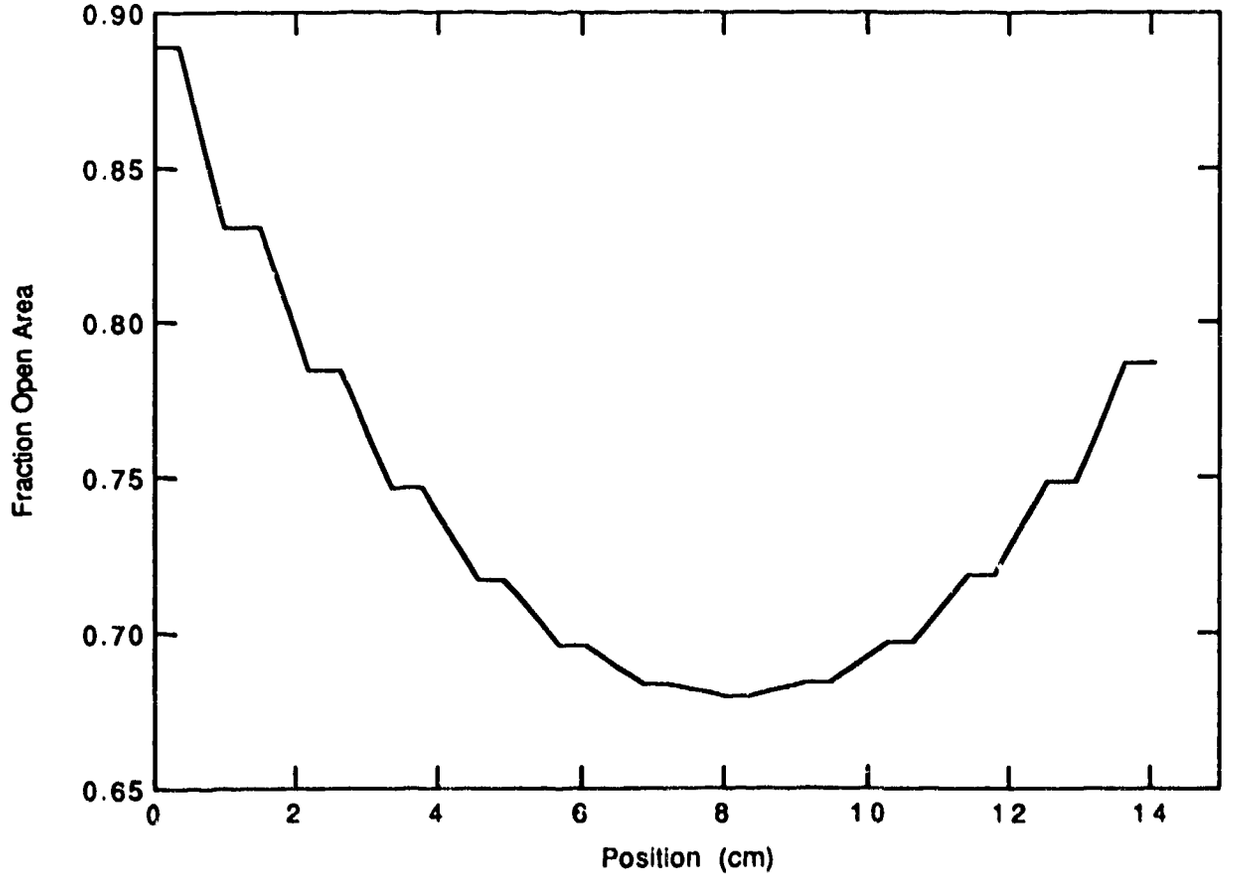

Figure 7. *Open aperture area vs. position in the detector for the x orientation of the slit.*

Figure 7 shows approximately how the transmission varies with y position for the "x" orientation. A minimum occurs at 8 cm from the center because of the decreasing height of the ribs and the spacing of the ribs.

The configuration of rib heights thus makes constant obscuration impossible. However, these shadows are present regardless of the size or configuration of the aperture. Small changes in the slit length to match either the maximum or minumum separation between the obscured bands does not significantly alter the range of open areas.

4. POSITION ACCURACY

We address the accuracy of source position determinations resulting from a single 24 hour pointing of the 2.56 cm x 0.5 cm slit aperture. We compute the spatial response of the detector to a uniform beam of X-rays, and subsequently fit the response to a "flat-top" Gaussian. The accuracy of the source position is then determined using the 90 % confidence level uncertainty in the position parameter. We further assume a number of minimally favorable conditions. We find that along the long dimension of the slit, position localization can be achieved to 0.5' diameter for a 10 millicrab source. With these parameters, localization in the short dimension is always less than 0.25'. With multiple pointings, the short dimension of the slit is projected onto a particular source in multiple ways, giving net position determination to 0.25' for orthogonally crossed slit projections.

4.1 Computational Algorithm

We require a more accurate point spread function to compute the position accuracies than for estimating the S/N. We thus construct the detector response to a uniform parallel x-ray beam by first calculating the number of photons incident on the detector due to the source, the sky background, and the internal background. Using a Monte Carlo approach, these counts are distributed uniformly on the detector. We modify these counting rates taking account of the effects mentioned in § 2, but treat them slightly differently.

Non-normal incidence, measured by an angle θ, enters as a strictly geometrical effect which reduces the aperture area by $\cos\theta$ for the source and diffuse background. It also affects the transformation from linear distance on the detector to angular distance on the sky. The angular position accuracy $\Delta\theta$ for a linear accuracy Δx is given by

$$\Delta\theta = \cos^2\theta \, \frac{\Delta x}{f} \qquad\qquad \Delta\theta = \cos\theta \, \frac{\Delta x}{f} \tag{15}$$

for illumination parallel and perpendicular to the length of the slit, respectively.

Absorption in the counter gas affects both source and diffuse sky photons. Here we express absorption in terms of the probability of transmission through a path length ℓ. In terms of a uniformly distributed random number r, this length is given by

$$\ell = -\frac{\cos\theta}{\tau} \ln r, \tag{16}$$

where $\tau = 1.36$ / cm, as before. If ℓ is greater than $1/\cos\theta$, then the path length is larger than the detector's depth, and photon is not recorded. In addition, the photon travels a horizontal distance $\ell \sin\theta$ in the detector, shifting the registering of the photon to a neighboring pixel.

Because the diffuse background is uniform and is stronger than the source for the source strengths we are considering, we simply decrease the number of counts due to the sky background by a factor of

$$1 - e^{-\tau/\cos\theta}. \tag{17}$$

The finite resolution of the detector is taken into account by shifting the position of the photon through the use of a Gaussian distributed random number having a distribution width equal to the detector resolution. Photons lying within the same detector pixel are then summed.

We calculate a 1-D projection of the intensity by summing the counts in the narrow direction. The width of this narrow direction, however, is important in determining the total number of background counts. This width we take from our studies of the signal-to-noise for a dim source, using the widu. giving the maximum S/N. We also take account that only a certain fraction of the counts distributed along this direction are included in the maximum S/N region. For an incident angle of 45 degrees and illumination along the length of the slit, this width is 0.5 cm. For an incident angle of 45 degrees and illumination perpendicular to the slit length, this width is 1.25 cm. In the long direction, parallel to the length of the slit, we use a length of 10.25 cm. The incident intensity of background counts is computed using areas of 5.125 cm^2 and 12.8125 cm^2, respectively.

This 1-D response function resulting from these effects is fit with a "flat-top" Gaussian function, which has the following form,

$$\begin{aligned} I &= Ce^{-((x_0-x_l-x)^2/2\sigma^2)} + B && x < x_0 - x_l \\ I &= Ce^{-((x_0+x_l-x)^2/2\sigma^2)} + B && x > x_0 + x_l \\ I &= C + B && x_0 - x_l < x < x_0 + x_l . \end{aligned} \tag{18}$$

x_o, x_l, σ, B and C are treated as free parameters. The position accuracy Δx is determined from the diameter of th: 90 % confidence error circle on x_o (*i.e* a change in χ^2 of 2.71[4]).

4.2 Results

Table 3 summarizes parameters fixed throughout our calculations. These include intensities for the backgrounds and the Crab for the energy range 3 - 6 keV, the spatial resolution of the detector and the integration time. Note that the number of steradians for the diffuse background is given by the ratio of the effective area and f^2. Table 4 gives results for position accuracies using the long dimension of the slit for a 10 mCrab source integrated for 1 day of observation. Shadowing by the Ti grate is expressed in terms of the fraction of open aperture area. The two entries for $\theta = 45°$ correspond to illumination along and perpendicular to the length of the slit, respectively (see Fig. 2). The $\Delta\theta$ listed is the average and standard deviation of the angular accuracy, computed from Eq. 15 using ~ 1000 separate realizations of the model. Figure 8 illustrates a typical point spread function and fit for illumination along the length of the slit.

Note that our choice of parameters are minimally favorable to locating the source. First, we have computed localizations using the long dimension of the slit. Source localization along the short dimension are always better than 0.25°. Further, we have assumed a single pointing in a 24 hour period. Multiple pointings, and hence, multiple slit orientations relative to the sky will improve the source localization. We have also used only a 3 - 6 keV energy range rather than the full 2 - 12 keV range, and have chosen the least absorptive energy for the counter gas. Further, the FWHM of the detector spatial resolution decreases with increasing energy, so a value of 0.5 cm is the worst detector resolution. At smaller FWHM values, the position accuracies would improve. Finally, we have chosen maximums in obscuration due to the Ti grate. With these conditions, the position of a 10 mCrab source can be determined to an accuracy of < 0.5°.

Comparing to position determination with the pinhole, in a 1 hr pointing the short dimension of the slit detemines the position of a 10 mCrab source at normal incidence to 0.96°, while the pinhole determines the position to 1.35°.

5. SUMMARY

We have shown the advantages of a slit aperture over the original pinhole design for MOXE. For steady sources, the slit is clearly better for locating sources than the pinhole. Since the narrow dimension of the slit better matches the position resolution of the detector, sources can be localized more accurately along the narrow dimension of the slit than along either axis of the pinhole. As the spacecraft changes its pointing several times per day, the slit will be projected on the source in various directions. The position accuracy in both sky dimensions will thus correspond to that derived from the narrow dimension of the slit, and be superior to a pinhole. In addition, the projections in various directions may serve to resolve some cases of source confusion. In rare instances when there is only one pointing of the satellite, the position of a 10mCrab source can be located to better than 0.5° along the long dimension of the slit. This accuracy is sufficient for the pointed instruments to locate the source for follow-on studies.

6. REFERENCES

1. Holt, S. S. and Priedhorsky, W. 1987, "All-sky Monitors for X-ray Astronomy," *Spa. Sci. Rev.*, **45**, 269 - 289.
2. Priedhorsky, W., Fenimore, E. E., Moss, C. E., Kelley, R. L., and Holt, S. S. 1989, "MOXE: an X-ray all-sky monitor for the Soviet Spectrum X-Gamma mission," *SPIE Proc.* Vol. 1159, *EUV, X-ray, and Gamma-Ray Instrumentation for Astronomy and Atomic Physics*. 177 - 189.
3. Matsuoka, M. 1990, "An X-ray All sky Monitor for Japanese Experiment Module on the Space Station," *I.A.U. Colloquium No. 123, "Observatories in Earth Orbit and Beyond,"*, in press.
4. Cash, W. 1976, "Generation of Confidence Intervals for Model Parameters in X-ray Astronomy," *Astr. Ap.*, **52**, 307 - 308.

Table 3
Constant Parameters for Position Error Calculation

Parameter	Value
1 Crab (3 - 6 keV)	1.4 photons cm^{-2} s^{-1}
Internal Background (3 - 6 keV)	0.003 photons cm^{-2} s^{-1}
Diffuse Sky Background (3 - 6 keV)	3.0 photons cm^{-2} s^{-1} sr^{-1}
Detector Resolution (FWHM)	0.5 cm
Integration time	86400 s

Table 4
Position Error along the Long Dimension of the Slit

Source Intensity (mCrab)	θ (°)	Fraction of Open Area	Detector Area (cm^2)	$\Delta\theta$ (′)
10.0	0.0	0.89	5.125	29.4 ± 4.6
10.0	45.0	0.68	5.125	21.8 ± 3.7
10.0	45.0	0.68	12.8125	27.6 ± 6.2

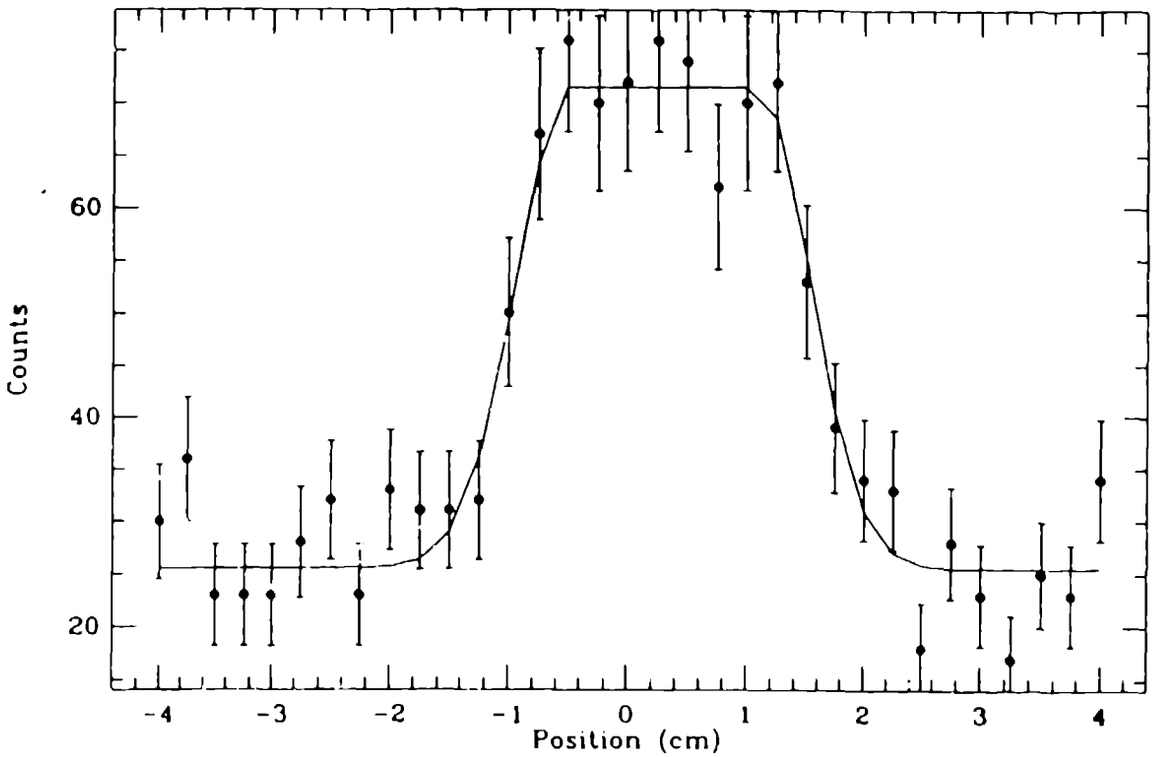

Fig. 8. The point spread function and resulting fit for one realization of a 10 mCrab source at an angle of incidence of 45°, with illumination parallel to the length of the slit. The total number of source counts recorded by the detector is 471, and the total number of internal and diffuse sky background counts are 1328 and 3105, respectively. The values for the fit parameters are (cf eq. 18):

$C = 46.0 \pm 4.4$ $\quad x_0 = 0.298 \pm 0.085$

$\sigma = 0.44 \pm 0.07$ $\quad x_1 = 0.79 \pm 0.09$

$B = 25.6 \pm 1.6$

χ^2 for the fit is 23.9, with 28 degrees of freedom. Errors on the parameters are 90 % confidence limits. The 0.085 cm error on x_0 corresponds to an error circle of 19.5 arc minutes.